

Cite this: DOI: 00.0000/xxxxxxxxxx

# Hydrodynamics of Multicomponent Vesicles Under Strong Confinement

Ashley Gannon,<sup>a</sup> Bryan Quaife,<sup>\*a</sup> and Y.-N. Young,<sup>\*b‡</sup>

Received Date

Accepted Date

DOI: 00.0000/xxxxxxxxxx

We numerically investigate the hydrodynamics and membrane dynamics of multicomponent vesicles in two strongly confined geometries. This serves as a simplified model for red blood cells undergoing large deformations while traversing narrow constrictions. We propose a new parameterization for the bending modulus that remains positive for all lipid phase parameter values. For a multicomponent vesicle passing through a stenosis, we establish connections between various properties: lipid phase coarsening, size and flow profile of the lubrication layers, excess pressure, and the tank-treading velocity of the membrane. For a multicomponent vesicle passing through a contracting channel, we find that the lipid always phase separates so that the vesicle is stiffer in the front as it passes through the constriction. For both cases of confinement, we find that lipid coarsening is arrested under strong confinement and proceeds at a high rate upon relief from extreme confinement. The results may be useful for efficient sorting lipid domains using microfluidic flows by controlled release of vesicles passing through strong confinement.

## 1 Introduction

Biological membranes, the basic structural units for compartmentalizing biological systems, comprise diverse arrays of proteins and lipid species. These lipids undergo phase separation, forming domains or rafts that lead to variations in material properties, including bending stiffness. Synthetic multicomponent vesicles, self-enclosed lipid bilayer membranes composed of different lipid species, have been used to study the rich patterns and accompanying morphologies that emerge from elastic heterogeneity in the membrane. In a quiescent environment, such elastic heterogeneity gives rise to wrinkling, budding, adhesion, and fusion of vesicle membranes<sup>1–3</sup>, closely related to several cellular processes<sup>4,5</sup>.

The hydrodynamics of a single-component vesicle is characterized by parameters such as the capillary number, reduced volume, and confinement ratio<sup>6</sup>. Such characterization is often useful for inferring fluid and material properties. For example, a vesicle's reduced volume and viscosity contrast determine if it undergoes tank-treading, swinging, or tumbling in a linear shear flow<sup>7</sup>. Transitions in the vesicle shape occur in non-linear parabolic flows<sup>8,9</sup>, and these shapes include axisymmetric bullets or parachutes, and asymmetric parachutes. Recently, characterization of vesicles suspended in a channel or pipe flow<sup>10–14</sup> showed more exotic vesicle hydrodynamics such as snaking and swirling behaviors in croissant and slipper shapes.

Under a linear shear flow, a multicomponent vesicle exhibits more exotic dynamics in both shape and membrane composition than a single-component vesicle<sup>15–21</sup>. For example, multicomponent vesicles under a background flow often exhibit highly complex morphologies, leading to vesicle budding. The hydrodynamics of these multicomponent vesicles include phase treading, tumbling with no viscosity contrast, swinging, budding, and fission<sup>15,21–25</sup>. Through numerical investigations, Liu *et al.*<sup>18</sup> identified several key dimensionless numbers, including the reduced area, capillary number, and the floppy-to-stiff ratio to characterize various dynamics of a two-dimensional multicomponent vesicle in an unbounded linear shear flow. In addition to the aforementioned numerical studies, these dynamics have been observed in experiments<sup>26–29</sup>.

Hydrodynamics of vesicles in extreme confinement have been studied as a model system for red blood cells (RBCs) squeezing through small capillaries (of sub-micron size in diameter) under a pressure difference<sup>30–33</sup>. Membrane permeability has been incorporated to examine the single-component vesicle hydrodynamics. In the absence of an osmotic gradient, the semipermeable vesicle is affected by water influx/efflux over a sufficiently long time or under a strong confinement<sup>12</sup>. Numerical simulations illustrate that a vesicle with moderate membrane permeability can go through a strong confinement much more easily, and can restore its water content within a very short time after its passage through the strong confinement. These results imply that the membrane permeability may be inferred from vesicle hydrodynamics under a strong confinement. Motivated by these results, in this work

<sup>a</sup> Department of Scientific Computing, Florida State University, Tallahassee, FL, 32306, USA. Email: bquaife@fsu.edu

<sup>b</sup> Department of Mathematical Sciences, New Jersey Institute of Technology, Newark, NJ, 07102, USA. Email: yyoung@njit.edu

we seek to investigate how strong confinement may affect the hydrodynamics of a multicomponent vesicle. This question is highly relevant to hydrodynamics of cells in a confinement, and to our knowledge has not been well studied. Ramachandran *et al.*<sup>34</sup> reported that confinement reduces the effective diffusion coefficient of the concentration fluctuation in multicomponent membranes. How is such a reduced concentration diffusion coefficient reflected in the hydrodynamics of multicomponent vesicles under strong confinement?

In this paper, we use numerical simulations and lubrication analysis<sup>35,36</sup> to investigate the effect of strong confinement on a two-dimensional multicomponent vesicle. In particular we show how the vesicle's reduced area and its lipid composition affect the dynamics in two strongly confined geometries. The remainder of the paper is organized as follows. Section 2 describes the model for the two-dimensional multicomponent vesicle. We introduce a new parameterization of the bending modulus that is necessary to avoid unphysical negative bending stiffness. Section 2.2 describes numerical methods and also defines the techniques we use to define the excess pressure, lubrication layer width, and tank-treading velocity. Section 3 demonstrates the effects of strong confinement on multicomponent vesicles. Finally, concluding remarks are made in Section 4.

## 2 Formulation

We consider a single multicomponent vesicle  $\omega$  with boundary  $\gamma$  suspended in a confined geometry  $\Omega \subset \mathbb{R}^2$  with boundary  $\Gamma$  (Figure 1). The fluid is assumed to have zero Reynolds number and is therefore governed by the incompressible Stokes equations

$$\nabla \cdot \mathbf{T} = 0 \quad \text{and} \quad \nabla \cdot \mathbf{u} = 0, \quad \mathbf{x} \in \Omega \setminus \gamma, \quad (1)$$

where  $\mathbf{T} = -p\mathbf{I} + \mu(\nabla \mathbf{u} + \nabla \mathbf{u}^T)$  is the hydrodynamic stress tensor,  $\mathbf{u}$  is the velocity,  $p$  is the pressure, and  $\mu$  is the fluid viscosity. Across the vesicle membrane, we require that the velocity is continuous and locally inextensible, and the membrane and hydrodynamic forces balance

$$[\mathbf{u}] = 0, \quad \nabla_\gamma \cdot \mathbf{u} = 0, \quad [\mathbf{T}\mathbf{n}] = \mathbf{f}, \quad \mathbf{x} \in \gamma, \quad (2)$$

where  $\mathbf{f}$  is the total membrane force and  $\mathbf{n}$  is the outward unit normal of  $\gamma$ . Parameterizing  $\gamma$  as  $\mathbf{x}(s, t)$ , where  $s$  is arclength and  $t$  is time, the no-slip boundary condition is  $\frac{d\mathbf{x}}{dt} = \mathbf{u}(\mathbf{x})$ . Along the solid wall  $\Gamma$ , we impose a Dirichlet boundary condition  $\mathbf{u}(\mathbf{x}) = \mathbf{U}(\mathbf{x})$ , where  $\mathbf{U}$  is a Hagen-Poiseuille flow at the inlet and outlet

$$\mathbf{U}(\mathbf{x}) = U \left( 1 - \left( \frac{y}{W} \right)^2 \right), \quad \mathbf{x} = (x, y) \in \Gamma, \quad (3)$$

and  $y \in [-W, W]$ .  $\mathbf{U}$  is zero along the top and bottom of the channel.

We nondimensionalize the governing equations with a characteristic length scale  $R_0 = 10^{-6}$  m, a maximum bending stiffness  $b_{\max} = 10^{-19}$  J, and fluid viscosity  $\mu = 5 \times 10^{-2}$  kg/ms. The resulting bending relaxation time scale is  $\mu R_0^3 / b_{\max} = 0.5$  s, the velocity scale is  $b_{\max} / \mu R_0^2 = 2$   $\mu\text{m/s}$ , the pressure scale is  $b_{\max} / R_0^3 = 10^{-1}$  Pa, and the tension scale is  $b_{\max} / R_0^2 = 10^{-7}$  N/m. The dimensionless parameters regarding the vesicle properties

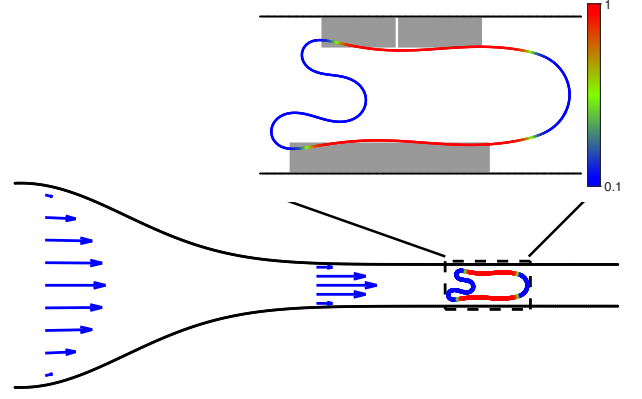


Fig. 1 A multicomponent vesicle suspended in a strongly-confined stenosis. The color is the dimensionless stiffness which varies from  $b_{\min} = 0.1$  to  $b_{\max} = 1$ . The vesicle dynamics are determined by a combination of phase, bending, and tension energies, and an imposed flow (blue arrows). The lubrication layer (gray region), defined in Section 2.4, plays a key role in the vesicle dynamics.

are the reduced area  $\alpha = 4\pi A / L^2$ , where  $A$  and  $L$  are the vesicle's area and length, respectively, and the floppy-to-stiffness ratio  $\beta = b_{\min} / b_{\max}$ . Since we consider flows in channels, we also define a maximum imposed velocity,  $U$ , which sets the capillary number  $Ca = UR_0^2 \mu / b_{\max}$ , and  $W / R_0$  is the dimensionless width of the channel which varies in both examples we consider. Finally, the Peclet number of the lipid dynamics is taken to be  $Pe = 1$  which results in a diffusion time scale of  $2 \times 10^{-4}$  s. Therefore, phase separation occurs at a rate three orders of magnitude faster than vesicle relaxation. The effect of the Peclet number has been examined<sup>15,18</sup>, and it has no qualitative effect on the vesicle dynamics. From this point onwards, all equations are dimensionless.

### 2.1 Constitutive equations

Using the model first introduced by Liu *et al.*<sup>18</sup>, the membrane forces depend on the Helfrich energy, line tension, and phase energy. The phase and bending energies are coupled through the bending modulus. In particular, the individual energies are

$$E_b = \frac{1}{2} \int_\gamma b(u) \kappa^2 ds, \quad E_t = \int_\gamma \sigma ds, \quad (4)$$

$$E_p = \frac{a}{\varepsilon} \int_\gamma \left( f(u) + \frac{\varepsilon^2}{2} |\nabla_\gamma u|^2 \right) ds, \quad (5)$$

where  $u$  is the dimensionless lipid concentration,  $b(u)$  is the lipid-dependent bending modulus,  $\sigma$  is the membrane tension,  $\kappa$  is the membrane curvature, and  $f(u) = \frac{1}{4} u^2 (1 - u)^2$  is a double-well potential with local minimums at  $u = 0$  and  $u = 1$ . The parameter  $\varepsilon \ll 1$  sets the size of the transition region of  $u$ , and the parameter  $a$  is line tension scaled by the characteristic bending stiffness. All simulations use the parameter values  $\varepsilon = 100$  and  $a = 0.04$ . The

resulting membrane forces are

$$\mathbf{f}_b = -(b(u)\mathbf{\kappa}\mathbf{n})_{ss} - \frac{3}{2} \left( b(u)\mathbf{\kappa}^2\mathbf{s} \right)_s, \quad \mathbf{f}_t = (\sigma\mathbf{s})_s, \quad (6)$$

$$\mathbf{f}_p = \left( \frac{a}{\varepsilon} \left( f(u) - \frac{\varepsilon^2}{2} u_s^2 \right) \mathbf{s} \right)_s, \quad (7)$$

where  $\mathbf{s}$  is the unit tangent vector of  $\gamma$ .

The lipid species  $u$  is governed by a fourth-order Cahn-Hilliard equation that results in the lipids phase separating while conserving their total mass. To model the variable bending, Sohn *et al.*<sup>15</sup> parameterized the bending modulus as

$$b(u) = (1 - u) + \beta u. \quad (8)$$

However, since the double-well potential does not have hard walls, the lipid concentration is not guaranteed to be confined to the interval  $[0, 1]$ . This is problematic since  $b(u) < 0$  if  $u > (1 - \beta)^{-1}$ , and such values of  $u$  are possible when  $\beta \ll 1$ ,  $Ca \gg 1$ , or the vesicle is confined to a narrow region. This behavior is demonstrated in Figure 2(a) for a vesicle with a floppy-to-stiff ratio  $\beta = 10^{-1}$  entering a stenosis. Using the linear bending model in Equation (8), the lipid concentration achieves a maximum value of  $u \approx 1.5$  which results in an instability that is formed by the resulting unphysical negative bending stiffness. To rectify this issue, we parameterize the bending modulus with the sigmoid function

$$b(u) = \frac{\beta - 1}{2} \tanh \left( 3 \left( u - \frac{1}{2} \right) \right) + \frac{\beta + 1}{2}. \quad (9)$$

This parameterization maps the local minimums of the double-well potential close to  $\beta$  and 1, but more importantly,  $b(u)$  remains bounded in  $(\beta, 1)$  even when  $u \notin [0, 1]$  (Figure 2(b)). We compare this new bending model against the linear model for a phase-treading and tank treading vesicle in Section 2.3.

## 2.2 Numerical Methods

We use a high-order integral equation formulation to resolve the complex vesicle shapes and long-range hydrodynamic interactions. The velocity field  $\mathbf{u}$  at  $\mathbf{x} \in \Omega$  is written as a combination of a single-layer potential and a double-layer potential

$$\mathbf{u}(\mathbf{x}) = S[\mathbf{f}](\mathbf{x}) + D[\eta](\mathbf{x}), \quad (10)$$

where

$$S[\mathbf{f}](\mathbf{x}) = \frac{1}{4\pi\mu} \int_{\gamma} \left( -\log \rho \mathbb{I} + \frac{\mathbf{r} \otimes \mathbf{r}}{\rho^2} \right) \mathbf{f}(\mathbf{y}) ds_{\mathbf{y}}, \quad (11)$$

$$D[\eta](\mathbf{x}) = \frac{1}{\pi} \int_{\Gamma} \frac{\mathbf{r} \cdot \mathbf{n}}{\rho^2} \frac{\mathbf{r} \otimes \mathbf{r}}{\rho^2} \eta(\mathbf{y}) ds_{\mathbf{y}}, \quad (12)$$

$\mathbf{r} = \mathbf{x} - \mathbf{y}$ ,  $\rho = |\mathbf{r}|$ , and  $\mathbb{I}$  is the  $2 \times 2$  identity matrix. The corresponding pressure is

$$p(\mathbf{x}) = \frac{1}{2\pi} \int_{\gamma} \frac{\mathbf{r} \cdot \mathbf{f}}{\rho^2} ds_{\mathbf{y}} + \frac{1}{\pi} \int_{\Gamma} \frac{1}{\rho^2} \left( \mathbb{I} - 2 \frac{\mathbf{r} \otimes \mathbf{r}}{\rho^2} \right) \mathbf{n} \cdot \eta ds_{\mathbf{y}}. \quad (13)$$

To avoid tangling, the vesicle membrane is parameterized in

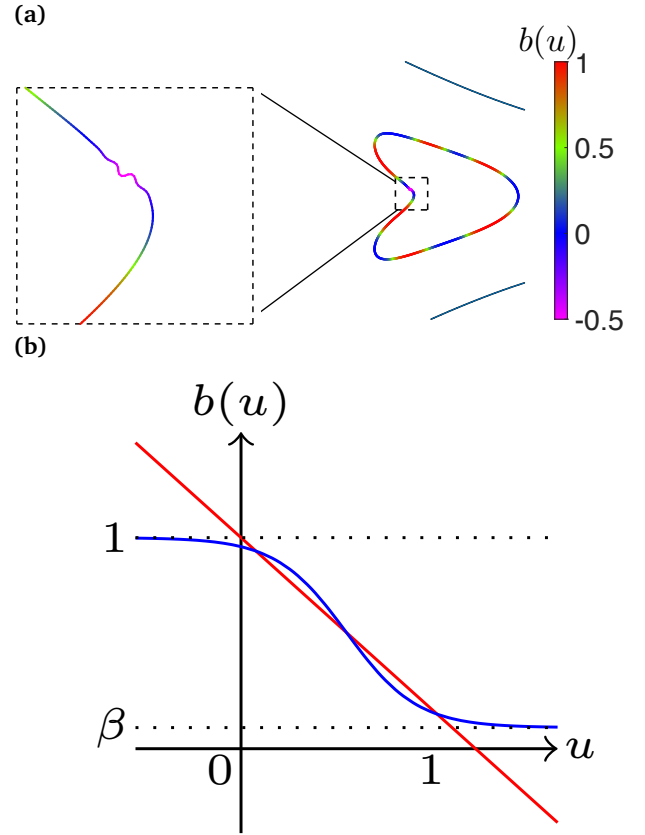


Fig. 2 (a) A multicomponent vesicle entering a closely-fitting channel (black lines) using the linear model in Equation (8). The color denotes the bending modulus  $b(u)$ . An instability is introduced where the vesicle bending modulus becomes negative. (b) The linear bending model in red (Equation (8)) and the new sigmoid bending model in blue (Equation (9)). Note that the new bending model satisfies  $b \in (\beta, 1)$  even if  $u \notin [0, 1]$ .

terms of the  $\theta$ - $L$  variables<sup>37</sup>, where  $L$  is the fixed vesicle length and  $\theta$  is the angle between the tangent vector and the positive  $x$ -axis. This requires decomposing the velocity field on  $\gamma$  into a normal velocity  $V$  and tangential velocity  $T$ . Then, the no-slip boundary condition for the vesicle velocity is

$$\frac{d\mathbf{x}}{dt} = V\mathbf{n} + T\mathbf{s} + D[\eta](\mathbf{x}), \quad \mathbf{x} \in \gamma. \quad (14)$$

The boundary condition on  $\Gamma$  is imposed by requiring that  $\eta$  satisfies

$$\mathbf{U}(\mathbf{x}) = -\frac{1}{2} \eta(\mathbf{x}) + S[\mathbf{f}](\mathbf{x}) + D[\eta](\mathbf{x}), \quad \mathbf{x} \in \Gamma. \quad (15)$$

The vesicle and solid walls are discretized at a set of collocation points. The single-layer potential is approximated using quadrature for weakly-singular integrands, while the double-layer potential is approximated using the spectrally accurate trapezoid rule. A high-order quadrature method resolves the hydrodynamic interactions between the vesicle and the solid wall<sup>38</sup>. Arclength derivatives are computed with spectral accuracy using Fourier methods. The resulting linear system is solved using GMRES. Finally, time stepping is carried out using the second-order Adams-Bashforth method.

### 2.3 Validation

We validate the new sigmoid bending model in Equation (9) by reproducing dynamics reported in the literature. Figure 3 shows a phase treading (top) and a tank-treading (bottom) multicomponent vesicle in an unconfined linear shear flow. The simulations align with the results reported by Liu *et al.*<sup>18</sup> (cf. Figure 3 and Figure 4).

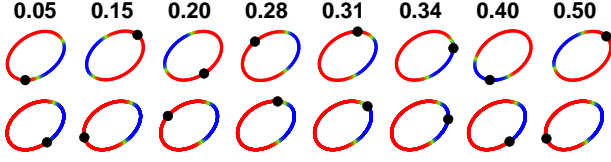


Fig. 3 A multicomponent vesicle in a linear shear flow undergoes phase treading (top) and tank-treading (bottom) with the new sigmoid bending model in Equation (9). The dimensionless times are in the title. The red region is stiff and the blue region is floppy. The simulations agree with the results in Liu *et al.*<sup>18</sup>.

### 2.4 Lubrication layers and excess pressure

The lubrication layer between a vesicle and the solid wall plays a critical role in the dynamics of a vesicle under strong confinement. Therefore, throughout Section 3, we calculate and analyze the flow inside the lubrication layers between the vesicle and the channel walls to elucidate the correlation between hydrodynamics and membrane dynamics. To define the size of the top lubrication layer, we let  $d(\mathbf{x}, \Gamma_{\text{top}})$  be the minimum distance between a point on the vesicle,  $\mathbf{x} \in \gamma$ , and the top half of the confining geometry. The size of the bottom lubrication layer is defined similarly. We find all local minimums of  $d(\mathbf{x}, \Gamma_{\text{top}})$ , with the condition that  $d(\mathbf{x}, \Gamma_{\text{top}}) < \delta$ , where  $\delta$  is a parameter. If no such local minimums exist, then the vesicle is too far from  $\Gamma_{\text{top}}$  to define a lubrication layer. If there are two or more local minimums, the left-most,  $\mathbf{x}_L$ , and right-most,  $\mathbf{x}_R$ , local minimums form the start and end of the lubrication layer. If there is only one local minimum, then  $\mathbf{x}_L$  and  $\mathbf{x}_R$  are the points on  $\gamma$  to the left and right of this local minimum with the condition that  $d(\mathbf{x}_L, \Gamma_{\text{top}}) = d(\mathbf{x}_R, \Gamma_{\text{top}}) = \delta$ . Then, the segment  $\gamma_{\text{layer}} \subset \gamma$  consists of all points  $\mathbf{x} \in \gamma$  between  $\mathbf{x}_L$  and  $\mathbf{x}_R$  with the condition that  $d(\mathbf{x}, \Gamma_{\text{top}}) < \delta$ . Finally, the lubrication layer width is

$$w_{\text{top}} = \frac{1}{|\gamma_{\text{layer}}|} \int_{\gamma_{\text{layer}}} d(\mathbf{x}, \Gamma_{\text{top}}) ds. \quad (16)$$

The region that defines the top and bottom lubrication layers is illustrated in Figure 1, and the height of the gray regions denote the lubrication layer thicknesses. In this example, the top layer is broken across two different regions.

A difference between the size of the top and bottom lubrication layers indicates that the vesicle membrane shape is asymmetric with respect to the center of the channel, and this results in tank-treading behavior<sup>11</sup>. To determine if a vesicle is tank-treading, we calculate the tangential velocity at several points on  $\gamma$ , and if this value is constant, this is the tank-treading velocity.

We also report the excess pressure for the stenosis geometry and relate it to the size of the lubrication layers. The excess pres-

sure is the additional pressure that is required to pass the vesicle through the geometry when compared to the pressure necessary if the vesicle were absent. Average pressures are calculated using Equation (13) along cross-sections that are parallel to the flow direction near the inlet and outlet of the stenosis.

## 3 Hydrodynamics of a multicomponent vesicle under strong confinement

We consider both a single-component and a multicomponent vesicle suspended in two geometries: a closely-fitting geometry (stenosis) and a geometry that slowly contracts to a narrow neck and then quickly widens (contracting). All the multicomponent examples have floppy-to-stiff ratio  $\beta = 10^{-1}$ . For the single-component case, we consider two bending stiffnesses:  $b(u) = 1$  and  $b(u) = 0.55$ . We refer to these cases as a stiff single-component vesicle and a floppy single-component vesicle, respectively. The smaller bending stiffness represents the average bending stiffness of a multicomponent vesicle, when its stiff and floppy regions cover the same amount of area. Throughout this section we plot the position of the vesicle in terms of the  $x$ -coordinate of its center of mass. For the stenosis geometry in Section 3.1, the narrow region begins at  $x = -15$  and ends at  $x = 15$ . For the contracting geometry in Section 3.2, the geometry begins to narrow at  $x = 4$  and reaches its narrowest point at  $x = 15$ .

### 3.1 A multicomponent vesicle in the stenosis geometry

We start by considering a vesicle with reduced area  $\alpha = 0.6$  passing through stenosis with a capillary number  $Ca = 0.25$ . With the current setup and  $Ca = 0.25$ , an elliptical vesicle with reduced area greater than  $\alpha = 0.8$  cannot fit through the closely-fitting geometry. Figure 4 shows six time steps of a (a) stiff single-component (b) floppy single-component, and (c) multicomponent vesicle. The lipid distribution of the multicomponent vesicle is initially random with a mean value of 0.55. In all plots, the color is the dimensionless bending modulus of the multicomponent vesicle that remains bounded in  $[0.1, 1]$  by using the new sigmoid bending modulus in Equation (9). A single Lagrangian point is included to visualize any tank-treading behavior. There are slight differences between the three cases, with the most noticeable being that the multicomponent vesicle has higher curvature in the floppy region. However, in general, there is little difference between these cases, principally because these vesicles have a large reduced area.

We next consider a vesicle with a smaller reduced area  $\alpha = 0.4$  with the same geometry and capillary number. Figure 5 shows the shape of a (a) stiff single-component, (b) floppy single-component, and (c) multicomponent vesicle at six locations along the stenosis channel. Contrary to the vesicles with the larger reduced area (Figure 4), the bending modulus has a large effect on the vesicle shape. We first consider the three different energies—bending, tension, and phase—for each example. In Figure 6, we plot these energies as a function of the vesicle's center. Note that the single-component vesicles do not have a phase energy. We observe that, as the vesicle enters the stenosis, it develops regions of high curvature, and this results in an increase in the bending en-



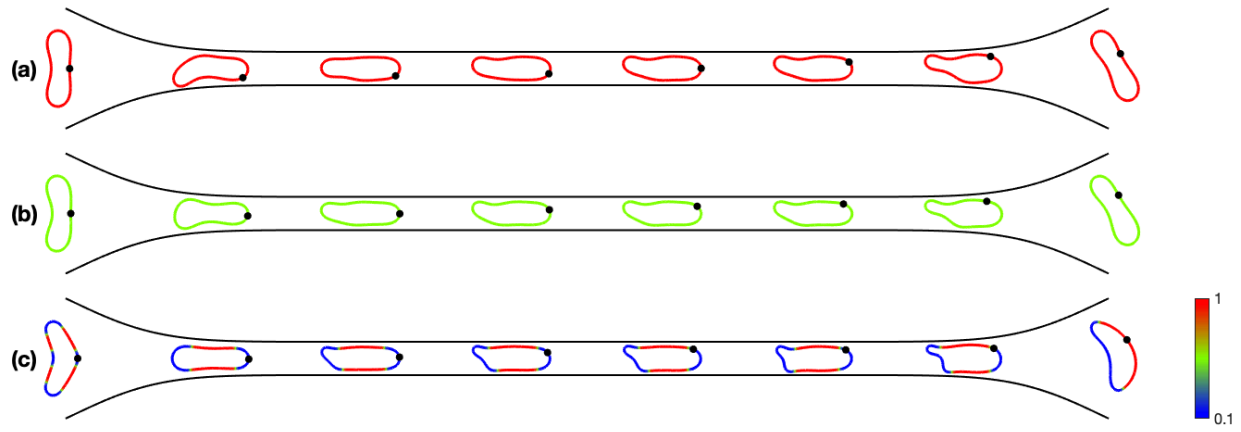


Fig. 4 A vesicle passing through the stenosis geometry. The vesicle's reduced area is  $\alpha = 0.6$  and the capillary number is  $Ca = 0.25$ . The vesicles are: (a) stiff single-component; (b) floppy single-component; (c) multicomponent.

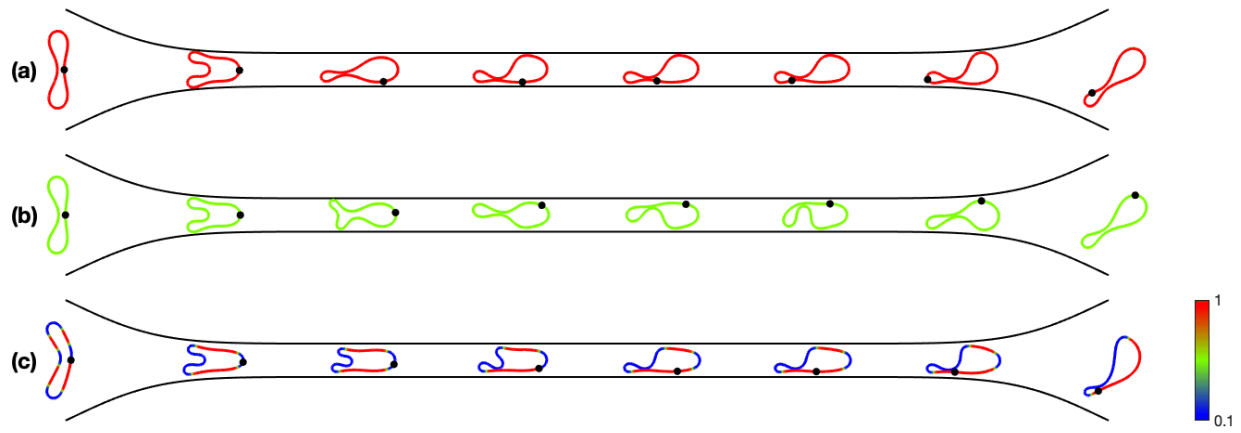


Fig. 5 A vesicle passing through the stenosis geometry. The vesicle's reduced area is  $\alpha = 0.4$  and the capillary number is  $Ca = 0.25$ . The vesicles are: (a) stiff single-component; (b) floppy single-component; (c) multicomponent.

ergy. As the stiff single-component and multicomponent vesicles reach a steady-state shape near the middle of the channel, their bending and tension energies remain nearly constant from  $x = 0$  until the end of the stenosis. For the multicomponent vesicle, the phase energy is also nearly constant in this region. This implies that there is no coarsening of lipid phase parameter in the middle of a stenosis.

The coexistence of multiple lipid domains in a vesicle under confinement results in additional interesting physics. We note that in Figure 6(c), the lipid species coarsens at three instances, and this results in a decrease in the phase energy. Each coarsening corresponds either to two stiff regions overtaking a small floppy region, or to two floppy regions overtaking a small stiff region. In the first case, a region that was originally floppy has become stiff, and this results in a sudden increase in the bending energy. In the latter case, because the mass of the lipid phase is conserved, the overtaken stiff region must relocate to the another stiff-floppy interface, and this also results in a sudden increase in the bending energy. These increases are visible in Figure 6(c) as small upticks in the blue curve. However, in both cases, the vesicle smooths out these new regions of high curvature, but it takes some time since the diffusion time scale is several orders of magnitude smaller

than the bending relaxation time scale.

Another difference between the two reduced areas is that the vesicles with smaller reduced area undergo tank-treading motions. As mentioned earlier, tank-treading occurs when the top and bottom lubrication layers differ in size. The size of the lubrication layers for all three cases of the vesicle with reduced area  $\alpha = 0.4$  are in the top half of Figure 7. The bottom of Figure 7 shows the tank-treading velocities of four Lagrangian points. The inset shows the vesicle configuration in the closely-fitting part of the channel, the black dashed line is the center line of the channel, the marks are the four Lagrangian points, and the rounded arrow denotes the direction of rotation. The stiff single-component and multicomponent vesicles are clearly tank treading. The direction and speed of the tank-treading depends on how much of the vesicle membrane is exposed to positive shear (below the center line) versus how much is exposed to negative shear (above the center line)<sup>8</sup>. The majority of the membrane of the stiff single-component and multicomponent vesicles are below the center line, and this results in a clockwise tank-treading behavior. In contrast, the majority of the membrane of the floppy single-component vesicle is above the center line, and the result is counterclockwise tank-treading. In addition, the tank-treading

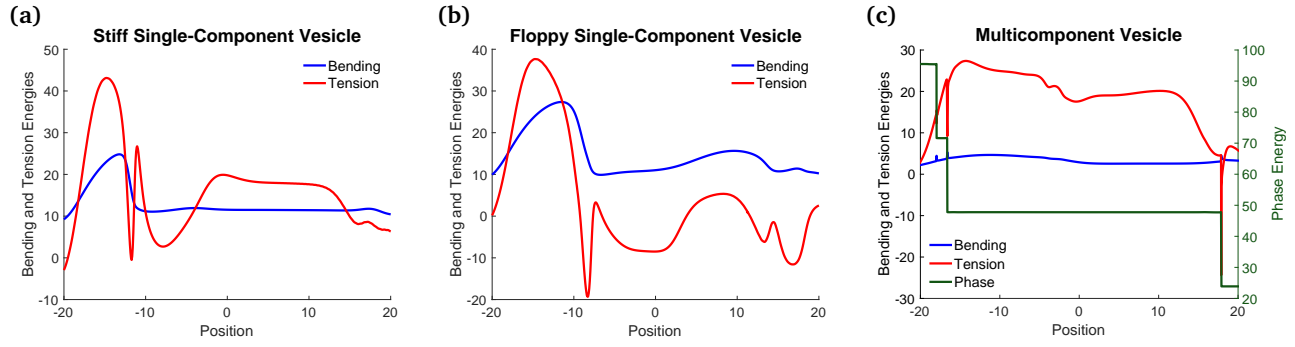


Fig. 6 The bending (blue), tension (red), and phase (green) energies of a (a) stiff single-component, (b) floppy single-component, and (c) multicomponent vesicle. The reduced area is  $\alpha = 0.4$ . Note that the single-component vesicles do not have a phase energy.

velocity can be correlated to the percentage of its membrane that is below the center line. We note, however, that the floppy single-component vesicle is still undergoing deformations, so the tangential velocities have not converged to a fixed value.

The sizes of the top and bottom lubrication layers are also related to the excess pressure. The green curve on the top half of Figure 7 shows the excess pressure (with the axis aligned on the right side of the plot). When the lubrication layers are large, most notably for the multicomponent vesicle, less pressure is required to force the vesicle through the geometry, and the result is a smaller (less negative) excess pressure. In contrast, when the lubrication layers are small, most notably for the stiff single-component vesicle, more pressure is required to force the vesicle through the geometry, and the result is a larger (more negative) excess pressure.

When a vesicle is tank-treading near a solid wall, the flow in the thin layer of fluid includes both a linear profile and a Poiseuille profile<sup>36</sup>. The magnitude of the Poiseuille profile is determined by the pressure gradient between the vesicle and the solid wall, while the linear profile is determined by the tangential velocity of the vesicle relative to the solid wall. Using the definition of the lubrication layer outlined in Section 2.4, we consider the flow profile inside this lubrication layer in Figure 8. We observe that the Poiseuille coefficient (quadratic term) can be either positive or negative, meaning that the pressure gradient in the streamwise direction in the lubrication layer switches signs. The Poiseuille coefficient is related to the lateral gradient of the tangential traction,  $\mathbf{F}_t$ , on the vesicle membrane<sup>39,40</sup>

$$\mathbf{F}_t = -\sigma_s + u_s \frac{\delta E^m}{\delta u}. \quad (17)$$

Here,

$$\frac{\delta E^m}{\delta u} = \frac{a}{\varepsilon} (f'(u) - \varepsilon^2 u_{ss}) + \frac{b'(u)}{2} \kappa^2 \quad (18)$$

is the derivative of the membrane energy with respect to the lipid concentration<sup>15</sup>.

For a single-component vesicle, the tangential traction is  $\mathbf{F}_t = -\sigma_s$  (the Marangoni stress), and the streamwise gradient of the Marangoni stress determines the sign of the Poiseuille coefficient in Figure 8(a). For a multicomponent vesicle, the Poiseuille coefficient can also change sign around the boundary between two

lipid domains, where the membrane energy changes sharply between lipid species. This correlation between the location of the boundary between lipid domains and the fluid velocity profile in the lubrication layer implies that, by visualizing the flow in the lubrication layer and identifying locations where the nonlinear shear flow profile is convex, it is possible to identify the location of boundaries between lipid domains as shown in Figure 8(b).

### 3.2 A multicomponent vesicle in the contracting geometry

In this section, we consider a vesicle passing through a channel that slowly contracts to a  $2 \mu\text{m}$  wide neck, and then immediately opens up to a channel that is ten times larger. We first consider the effect of the initial lipid concentration when the floppy and stiff regions each make up half of the vesicle membrane. In Figure 9, snapshots of vesicles with reduced area  $\alpha = 0.5$  with different initial lipid distributions are illustrated. The initial distributions are (a) random, (b) stiff in the front and floppy in the back, and (c) floppy in the front and stiff in the back. The vesicle with the random initial lipid distribution quickly phase separates into two floppy and two stiff regions. As seen in the stenosis geometry, further phase separation is delayed until the vesicle is no longer under strong confinement. The vesicle with the stiff region at the front maintains its orientation. In contrast, the vesicle with the floppy region on the front reorients the floppy region towards the back of the vesicle. In summary, in all three cases, the vesicle is orienting itself so that the stiff region passes through the constriction before the floppy region. Therefore, in subsequent simulations, we initialize the vesicle's lipid concentration so that the floppy region is in the back and its stiff region is in the front. The vesicle shapes develop regions with high curvature in the floppy region when they first pass through the narrowest part of the geometry, but once the strong confinement is abruptly removed, these regions of high curvature are quickly smoothed.

In addition to the lipid distribution, the percentage of the vesicle that is floppy plays a role in the vesicle shapes and dynamics. Therefore, we consider a vesicle with reduced area  $\alpha = 0.5$  in the contracting geometry with various sizes of the floppy region. Motivated by the last experiment, we initialize the stiff region to be in the front and the floppy region to be in the back. In each simulation, the capillary number is  $Ca = 0.25$ . Figure 10 shows the vesicle shapes at the same six time steps when the percent-

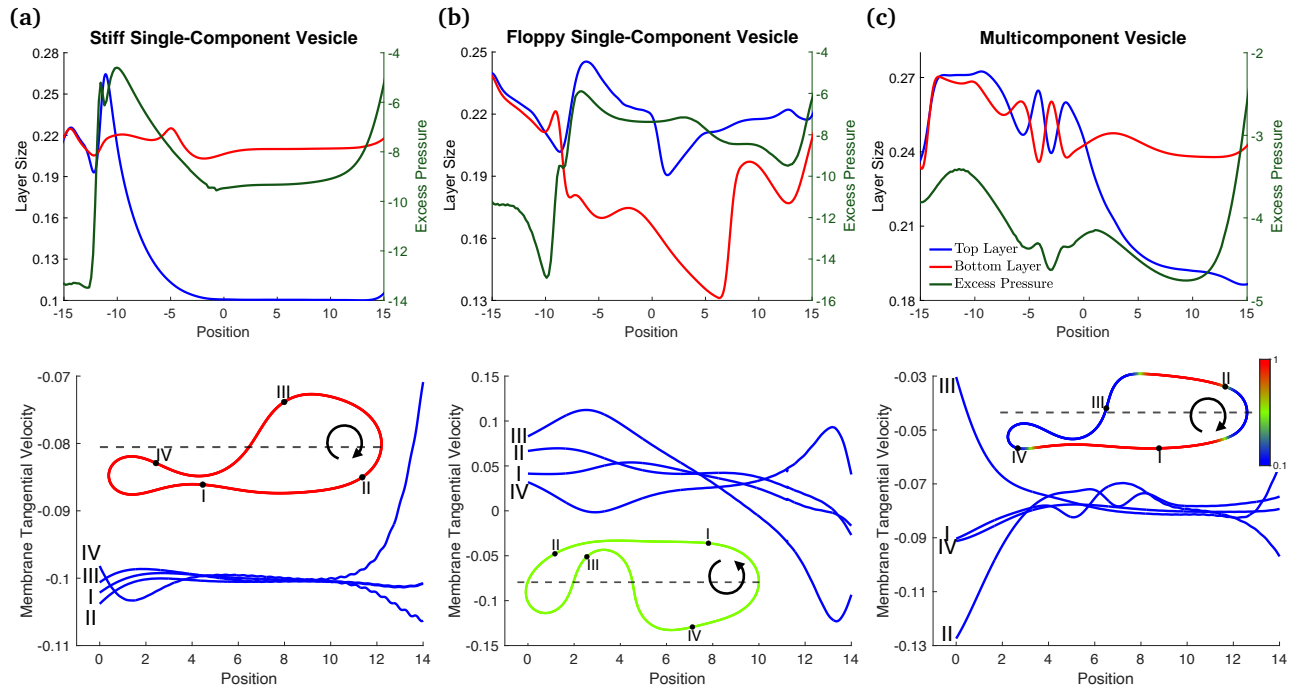


Fig. 7 The lubrication layer thicknesses (red and blue), excess pressure (green), and tank-treading velocity of four Lagrangian points of a (a) stiff single-component vesicle, (b) floppy single-component vesicle, and (c) multicomponent vesicle. The reduced area is  $\alpha = 0.4$  in all three cases. Also illustrated is the vesicle shape and the four Lagrangian points at the location indicated by the dash line. The black dashed line is the center line of the channel, and the arrow denotes the tank-treading direction. The percentage of the vesicle membrane that is below the center line is (a) 72%, (b) 44%, and (c) 68%.

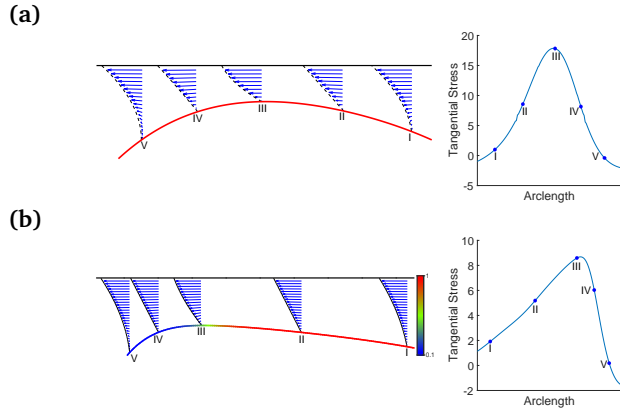


Fig. 8 The co-moving velocity field in the thin fluid layer between the top of a vesicle and the stenosis geometry. The vesicles are (a) stiff single-component; (b) multicomponent. Similar velocity profiles between the bottom of the vesicle and the stenosis geometry. The profiles are plotted at slices where the pressure gradient transitions from a value that is negative, zero, positive, zero, and negative. The right plots show the tangential stress with the five slices denoted by the marks. Note that the reversal in the pressure gradient occurs when the tangential stress is sufficiently large.

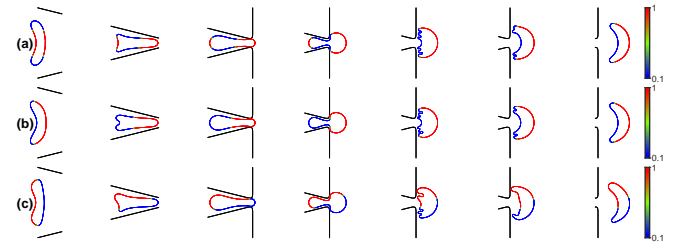


Fig. 9 A multicomponent vesicle with 50% floppy region passing through a contracting geometry. The vesicle's reduced area is  $\alpha = 0.5$  and the capillary number is  $Ca = 0.25$ . The lipid distribution is initialized to be (a) random, (b) phase separated with the stiff region leading; (b) random; (c) phase separated with the floppy region leading.

age of the floppy region is (a) 0% (single-component), (b) 15%, (c) 25%, (d) 35%, and (e) 45%. One effect of the size of the floppy region is that the symmetry of the vesicle shape is broken at smaller percentages. We also see that floppier vesicles have faster migration speeds, but the effect is quite small—Table 1 reports the time the vesicle first passes through the neck.

Floppy percentage	0%	15%	25%	35%	45%	50%
Dimensionless time	2.32	2.30	2.29	2.26	2.23	2.25

Table 1 The time required for the vesicles to completely pass through the neck.

We conclude this example by considering the different shapes and energies that single-component and multicomponent vesicles display. Since we have initialized the lipid species to initially

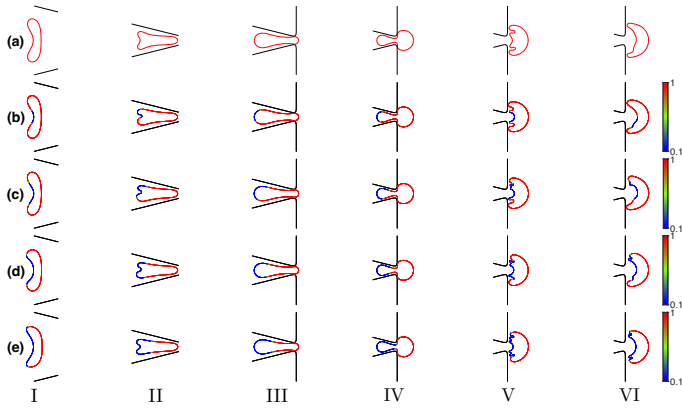


Fig. 10 A vesicle passing through a contracting geometry. The vesicle's reduced area is  $\alpha = 0.5$  and the Capillary number is  $Ca = 0.25$ . (a) A stiff single-component vesicle. The percentage of the multicomponent vesicle that is floppy is (b) 15%, (c) 25%, (d) 35%, and (e) 45%. The vesicles with a larger percentage of floppy regions pass through the neck earlier than the vesicles with less percentage of floppy regions.

be phase separated, the phase energy is nearly constant for all cases, and is therefore not plotted. The tension energy, on the other hand, increases as the vesicle approaches the neck, but its general shape is similar for all five cases, and it too is not plotted. However, the bending energies show different behaviors for each of the cases (Figure 11). The main difference being that the multicomponent vesicles with a higher percentage of floppy regions have less bending energy, especially as the vesicle passes through the neck. We also note that the bending energy undergoes several transient increases and decreases. These occur when the tail of the vesicle undergoes transitions from lower energy shapes, such as 'C' or 'S' shapes, to high energy shapes, such as 'W' shapes. Figure 12 shows these different vesicle shapes for the single-component vesicle and multicomponent vesicle that is 45% floppy. The shapes at several critical points along the bending energy are included.

## 4 Conclusions

In this work we used numerical simulations to examine the hydrodynamics of a multicomponent vesicle under strong confinement. The vesicle is an simplified model for a red blood cell, which has multiple lipid domains in its membrane and often has to squeeze through a small space. We refined the phase-field formulation in Liu *et al.*<sup>18</sup> with a new bending model that uses a sigmoid function for the bending stiffness to retain positiveness in the bending modulus. The linear model<sup>18</sup> works well for a vesicle in free-space. However, under strong confinement we find it necessary to enforce the condition that the dimensionless bending modulus  $b(u)$  be in the range of  $[\beta, 1]$  ( $\beta = b_{\min}/b_{\max}$ ) to avoid instability in membrane shapes (see § 2.1). We focused on the hydrodynamics of a multicomponent vesicle in two types of confinement: a stenosis channel (§ 3.1), and a contracting channel (§ 3.2). For both confining geometries we varied the reduced area  $\alpha$  and the initial distribution of lipid domains with a fixed floppy-to-stiff ratio  $\beta = 0.1$ , a fixed Capillary number  $Ca = 0.25$ , and a fixed Peclet number of the lipid dynamics  $Pe = 1$ .

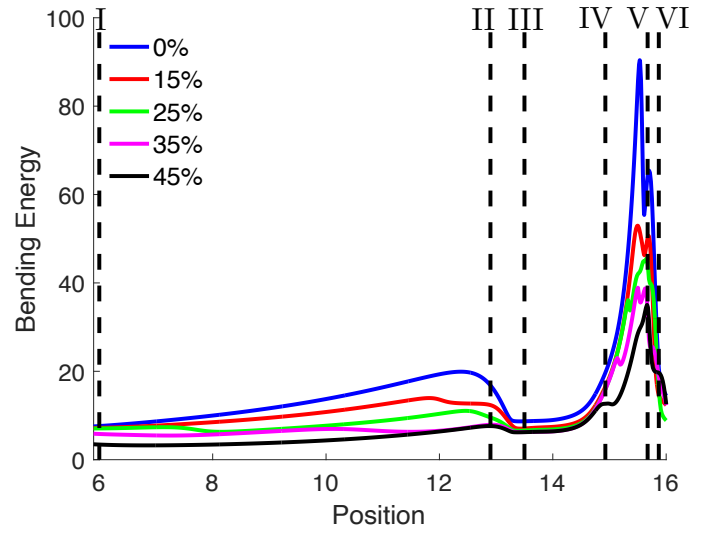


Fig. 11 The bending energies of the single-component and multicomponent vesicles in Figure 10. The vertical dashed lines correspond to the configurations in Figure 10. As the size of the floppy region increases, the maximum bending energy decreases.

In § 3.1 the confinement ratio (defined as  $2R_0/W$ ) in the stenosis is 1.67, and in § 3.2 the confinement ratio increases to a maximum of 3.60 at the neck. Consequently the dependence of the vesicle shape on the capillary number is expected to be less sensitive according to results in Agarwal and Biros<sup>11</sup>. Finally the phase separation is assumed to occur at a much faster time scale than vesicle relaxation with Peclet number  $Pe = 1$ .

As a multicomponent vesicle enters and exits a closely-fitted stenosis, coarsening of the lipid domains is expedited. However, inside the stenosis, the strong confinement hinders the coarsening as the vesicle shape and the lipid distribution remain nearly unaltered as the vesicle moves through the stenosis. Once inside a stenosis, we define the lubrication layer and its width. We find that tank-treading along the vesicle inside the stenosis is closely related to the asymmetry in the lubrication layer width between the top and bottom walls. For vesicles with a high reduced area the lubrication layer width is symmetric between the top and bottom walls, and we find no tank-treading along the membrane. On the other hand, for a vesicle with a lower reduced area, the lubrication layer width is asymmetric and the vesicle membrane tanks treads. Furthermore we also find that the excess pressure (the additional pressure required to pass the vesicle through the stenosis) is correlated to the size of the lubrication layer: a larger lubrication layer size results in a smaller excess pressure.

Inside the lubrication layer, the shear flow consists of a quadratic component (due to pressure gradient in the thin film) and a linear component (due to membrane motion in the tangential direction). By analyzing these two components at various locations in the lubrication layer, we further elucidated the correlation between the location of boundary between lipid domains and the change of sign in the pressure gradient in the lubrication layer. These results may be used to identify the location of boundaries between the lipid domains via the visualization of the flow in the lubrication layer.

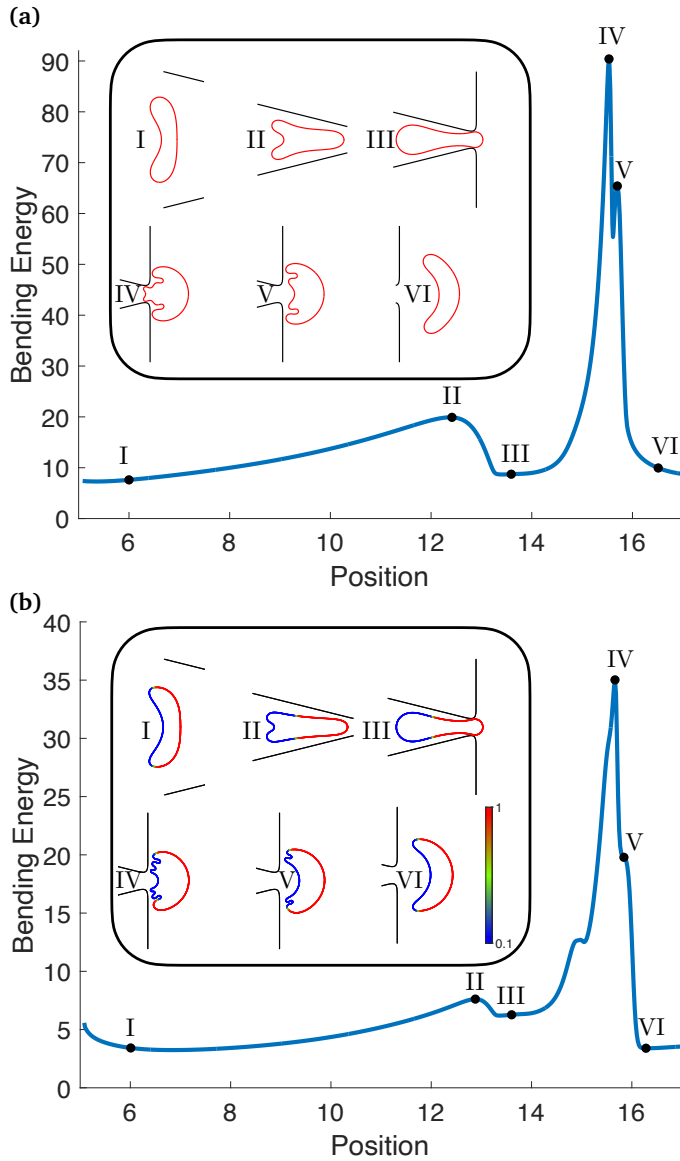


Fig. 12 The bending energy of (a) a stiff single-component vesicle, and (b) a multicomponent vesicle whose boundary is 45% floppy passing through a contracting geometry. The vesicle shape at different locations are included. We can clearly see that the sudden increases and decreases in the bending energy are due to transitions between lower energy and higher energy shapes.

For a multicomponent vesicle squeezing through a constriction, we simulated the passage of a vesicle with various initial configurations of lipid domains. We found that, once the vesicle makes its passage, the front of the vesicle is often stiffer than the back of the vesicle, with a similar shape of a smaller curvature in the front than the curvature in the back. This is also observed for a vesicle moving out of confinement from a stenosis channel. Thus we propose that a strong confinement followed by a sharp transition to a wider opening can be used to produce phase-separated multicomponent vesicle with the floppy lipid species in the back and the stiff lipid species in the front of the vesicle.

Such asymmetry in lipid domain induced by strong confine-

ment and sudden release gives rise to a nonuniform tension distribution in the membrane, with a smaller tension (in magnitude) in the front and a larger tension (in magnitude) in the back. This resembles the behavior of a red blood cell as it traverses a narrow slit<sup>31</sup>. During this process, the membrane tension is primarily negative, resulting in compression that is more pronounced at the rear of the cell than at the front.

## Author Contributions

Conceptualization: AG, BQ, YNY; methodology: AG, BQ, YNY; validation: AG, BQ, YNY; formal analysis: AG, BQ, YNY; investigation: AG, BQ, YNY; data curation: AG, BQ, YNY; writing - original draft: AG, BQ, YNY; writing - review and editing: BQ, YNY; visualization: AG, BQ, YNY; supervision: BQ, YNY; project administration: BQ, YNY; funding acquisition: BQ, YNY

## Conflicts of interest

There are no conflicts to declare.

## Acknowledgements

We thank David Salac for discussions, and Shuwang Li for discussions and sharing his code for a multicomponent vesicle in free space. B.Q. acknowledges support from the Simons Foundation, Mathematics and Physical Sciences-Collaboration Grants for Mathematicians, Award No. 527139. Y.-N.Y. acknowledges support from NSF (Grants No. DMS 1614863 and No. DMS 195160) and Flatiron Institute, part of Simons Foundation.

## Notes and references

- 1 J. S. Lowengrub, A. Ratz and A. Voigt, *Physical Review E*, 2009, **79**, 031926.
- 2 S. Li, J. Lowengrub and A. Voigt, *Communications in Mathematical Sciences*, 2012, **10**, 645–670.
- 3 Y. Zhao and Q. Du, *Physical Review E*, 2011, **84**, 011903.
- 4 C. Rauch and E. Farge, *Biophysics Journal*, 2000, **78**, 3036–3047.
- 5 M. Takeda, G. P. Leser, C. J. Russel and R. A. Lamb, *Proceedings of the National Academy of Science*, 2003, **100**, 14610–14617.
- 6 D. Abreu, M. Levant, V. Steinberg and U. Seifert, *Advances in Colloid and Interface Science*, 2014, **208**, 129–141.
- 7 H. Noguchi and G. Gompper, *Physical Review E*, 2005, **72**, 011901.
- 8 B. Kaoui, G. Biros and C. Misbah, *Physical Review Letters*, 2009, **103**, 188101.
- 9 G. Danker, P. M. Vlahovska and C. Misbah, *Physical Review Letters*, 2009, **102**, 148102.
- 10 J. Lyu, P. G. Chen, A. Farutin, M. Jaeger, C. Misbah and M. Leonetti, *Physical Review Fluids*, 2023, **8**, L021602.
- 11 D. Agarwal and G. Biros, *Physical Review Fluids*, 2020, **5**, 013603.
- 12 B. Quaife, A. Gannon and Y.-N. Young, *Physical Review Fluids*, 2021, **6**, 073601.
- 13 M. Abbasi, A. Farutin, A. Nait-Ouhra, H. Ez-Zahraouy, A. Benyoussef and C. Misbah, *Physical Review Fluids*, 2022, **7**, 093603.



- 14 X. Wang, S. Ii, K. Sugiyama, S. Noda, P. Jing, D. Liu, X. Che and X. Gong, *Physics of Fluids*, 2023, **35**, 031910.
- 15 J. S. Sohn, Y.-H. Tseng, S. Li, A. Voigt and J. S. Lowengrub, *Journal of Computational Physics*, 2010, **229**, 119–144.
- 16 K. A. Smith and W. E. Uspal, *Journal of Chemical Physics*, 2007, **126**, 02B610.
- 17 G. Cox and J. Lowengrub, *Nonlinearity*, 2015, **28**, 773–793.
- 18 K. Liu, G. R. Marple, S. Li, S. Veerapaneni and J. Lowengrub, *Soft Matter*, 2017, **13**, 3521–3531.
- 19 S. Tusch, E. Loiseau, A.-H. A. H., K. Khelloufi, E. Helfer and A. Viallat, *Physical Review Fluids*, 2018, **3**, 123605.
- 20 P. Gera and D. Salac, *Soft Matter*, 2018, **14**, 7690–7705.
- 21 P. Gera, D. Salac and S. E. Spagnolie, *Journal of Fluid Mechanics*, 2022, **935**,.
- 22 X. Wang and X. Du, *Journal of Mathematical Biology*, 2008, **56**, 347–371.
- 23 J.-M. Allain and M. B. Amar, *The European Physical Journal E*, 2006, **20**, 409–420.
- 24 R. Lipowsky, *Journal de Physique II*, 1992, **2**, 1825–1840.
- 25 T. S. Ursell, W. S. Klug and R. Phillips, *Proceedings of the National Academy of Science*, 2009, **106**, 13301–13306.
- 26 L. Bagatolli and P. B. S. Kumar, *Soft Matter*, 2009, **5**, 3234–3248.
- 27 M. Yanagisawa, M. Imai and T. Taniguchi, *Physical Review E*, 2010, **82**, 051928.
- 28 M. Yanagisawa, M. Imai and T. Taniguchi, *Physical Review Letters*, 2008, **100**, 148102.
- 29 Y. Dreher, K. Jahnke, E. Bobkova, J. P. Spatz and K. Göpfrich, *Angewandte Chemie*, 2021, **60**, 10661–10669.
- 30 J. B. Freund, *Physics of Fluids*, 2013, **25**, 110807.
- 31 H. Lu and Z. Peng, *Physics of Fluids*, 2019, **31**, 031902.
- 32 P. G. Chen, J. M. Lyu, M. Jaeger and M. Leonetti, *Physical Review Fluids*, 2020, **5**, 043602.
- 33 A. Gürbüz, O. S. Pak, M. Taylor, M. V. Sivaselvan and F. Sachs, *Biophysics Journal*, 2023, **122**, 1–12.
- 34 S. Ramachandran, S. Komura, K. Seki and M. Imai, *Soft Matter*, 2011, **7**, 1524–1531.
- 35 Y.-N. Young and H. A. Stone, *Physical Review Fluids*, 2017, **2**, 064001.
- 36 P. Mistriotis, E. O. Wisniewski, K. Bera, J. Keys, Y. Li, S. Tuntithavornwat, R. A. Law, N. A. Perez-Gonzalez, E. Erdogan, Y. Zhang, R. Zhao, S. X. Sun, P. Kalab, J. Lammerding and K. Konstantopoulos, *Journal of Cell Biology*, 2019, **218**, 4093–4111.
- 37 T. Y. Hou, J. S. Lowengrub and M. J. Shelley, *Journal of Computational Physics*, 1994, **114**, 312–338.
- 38 B. Quaife and G. Biros, *Journal of Computational Physics*, 2014, **274**, 245–267.
- 39 A. Oron, S. H. Davis and S. G. Bankoff, *Rev. Mod. Phys.*, 1997, **69**, 931–980.
- 40 Y.-N. Young, S. Veerapaneni and M. J. Miksis, *J. Fluid Mech.*, 2014, **751**, 406–431.